(Received 29 July 2024, Accepted 14 October 2024, Scheduled 23 October 2024)

# Implementation of Fractal Metamaterial Inspired Antenna for Multi-Standard Wireless Applications

Hareetaa Mallani[1,*], Archana Agrawal[1], and Ritesh K. Saraswat[2]

[1]*Sangam University, Bhilwara (Rajasthan), India*
[2]*M.L.V.Textile & Engineering College, Bhilwara (Rajasthan), India*

**ABSTRACT:** In this article, a fractal slotted metamaterial inspired multiband antenna for wireless communication applications is presented. The proposed structure incorporates the fractal formation of a radiating patch attached with metamaterial SRR cell and rectangular slotted partial ground plane to cover multiple wireless standards. The antenna is printed on FR4 epoxy substrate material having the thickness of 1.6 mm and relative permittivity of 4.4. The antenna has compactness in size as $37 \times 22 \times 1.6\,\text{mm}^3$ and achieves five wireless communication modes, including S band (2.4 GHz; WLAN: IEEE 802.11g), S band (3.65 GHz; WiMAX: IEEE 802.16e), C band (5.0/5.8 GHz; WLAN: IEEE 802.11a/j), X-band (Satellite communication, radar, terrestrial broadband, space communication), 5G NR bands (n41: 2.496–2.690 GHz, n46: 5.15–5.925 GHz, n47: 5.855–5.925 GHz, n53: 2.483–2.495 GHz, n102: 5.925–6.425), and Lower Ku band (Molecular rational spectroscopy). The antenna also showcases consistent radiation characteristics, gain, and efficiency across resonant bands crucial for obtained resonant bands regarding multi-standard wireless applications. It attains an optimized peak gain of 4.38 dBi and a radiation efficiency of 86.23%.

## 1. INTRODUCTION

Lately, research has been intensely directed towards advancing wireless communication systems with metamaterial-inspired multiband antennas. This emphasis stems from the pursuit of smaller sizes, faster data transmission, and economical solutions. A plethora of multiband antennas have been developed for wireless standards such as WLAN/WiMAX. In today's fast-paced wireless communication landscape, there is a critical demand for antennas that can operate across multiple bands within a single design, enabling the smooth functioning of various wireless applications. Achieving a multiband configuration for antennas involves employing techniques like slotting, fractal formation, feeding, and more. By utilizing these techniques, either separately or in hybrid combinations, it becomes possible to design a multiband antenna capable of serving a wide range of wireless applications. The adoption of multiple operating antenna designs inspired by Metamaterials (MTM) has gained significant traction due to their heightened adaptability in capturing diverse electromagnetic phenomena in today's era.

Achieving multiple band configurations involves various approaches, including feeding methods [1–3], slot formation [4–9], loading metamaterial cells [10–14], fractal geometry insertion [15], and others. Incorporating slots into antenna structure facilitates miniaturization as well as enables multiband functionality regarding wireless standards, primarily influenced by the effects of current perturbation [16–18]. The metamaterial (MTM) structure exhibits unique properties of negative permeability and permittivity, significantly affecting dielectric constants. These characteristics play a crucial role in enhancing electromagnetic wave propagation and are instrumental in designing multiband antennas [58–60]. Various designs have been proposed to cover applications in millimeter- and terahertz-wave communication, particularly for photodetectors. Topological insulators (TIs) are considered promising candidates for long-wavelength photodetection due to the presence of Dirac fermions in their topologically protected surface states [61–70].

Ref. [19] proposes a multiple resonating antenna that utilizes a metamaterial inspired approach to cover WLAN/WiMAX applications. Discoveries in [20–22] showcase metamaterial-implemented multiband structures that cater to a range of wireless communication modes. Furthermore, [23] presents a compact quad-band antenna that incorporates a slotted and fractal geometry with metamaterial cell. Combining MTM characteristics with a fractal approach is advocated for numerous antenna designs, with the goal of attaining multiband capabilities and enhanced radiation properties [24–26]. Ref. [27] illustrates an antenna with a fractal geometry coupled with an MTM ground, catering to various wireless applications. For size compactness and bandwidth enhancement, fractal antennas with MTM cell are proposed in [28–32]. In [33], a multiple resonating antenna for multiple wireless standards is introduced, utilizing the Defected Ground Structure (DGS) approach within its design. Refs. [34, 36] discuss the implementation of fractal geometric structures within the patch area to achieve multiple resonant modes, enabling the support of various wireless applications. The multiple unit wideband MIMO antenna array approach is relevant for mobile devices seeking bandwidth improvement and compatibility with 5G NR communication bands [42, 46].

* Corresponding author: Hareetaa Mallani (hareetaa@mlvti.ac.in).

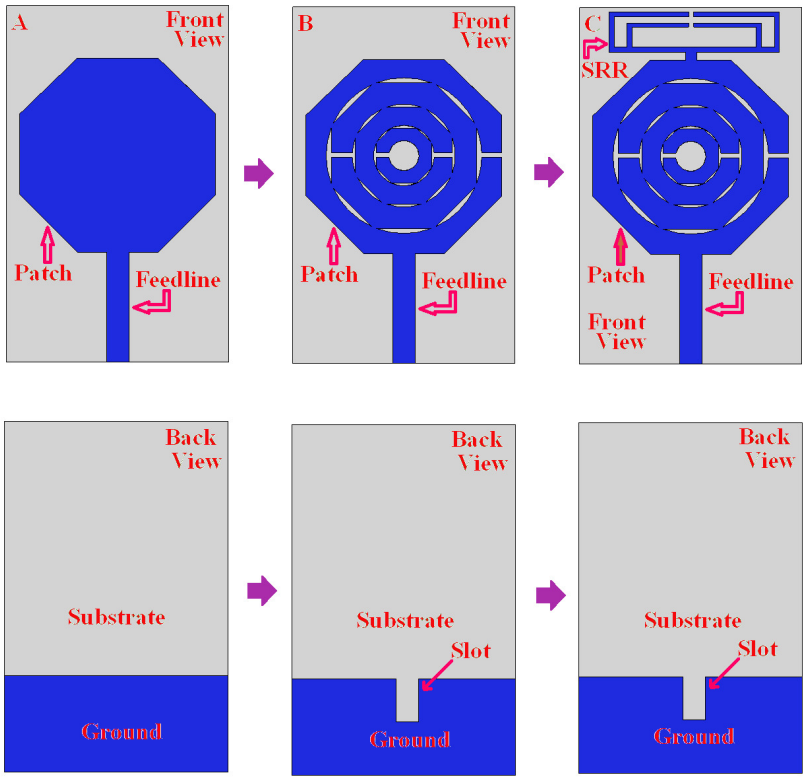


**FIGURE 1**. Proposed structure design evolutionary steps.

A slot-antenna array with wideband and high isolation, designed on an FR4 substrate, caters to multiple-input multiple-output (MIMO) systems to cover the fifth-generation new radio (5G NR) communication bands N77/N78/N79 [45]. Additionally, a dual-band low-profile quad-port printed antenna is proposed for 5G applications, utilizing the 5G spectrum between 3.3 and 3.8 GHz, particularly in the n77 band, with a 10 dB impedance bandwidth [47].

This paper presents a design for a metamaterial multiband antenna featuring a slotted SRR-based radiating section coupled with a rectangular split ring resonator (SRR) cell and a slotted rectangular ground plane. The proposed design operates in penta-band resonating mode, covering WiMAX at 3.65 GHz, WLAN at 2.4, 5.0, 5.8 GHz, entire X band (8–12 GHz), lower range of $K_U$ band, and 5G Sub-6 GHz NR Bands (5G FR1). The proposed design offers several benefits and novel features.

(i) The multiband capability is achieved by incorporating a fractal-based radiating section with rectangular SRR loading. (ii) The use of a slotted rectangular DGS approach with an SRR cell enables the antenna to resonate across bands suitable for 5G New Radio portable devices and wireless applications, including WLAN, WiMAX, X-band, and $K_U$-band. (iii) The proposed design is compact, fabricated on a low-cost FR-4 substrate, and easily implementable for 5G wireless applications.

The paper is organized into four sections. Section 2 deals with the design process of the proposed metamaterial penta-band antenna. Section 3 mentioned the design and analysis of the metamaterial Split Ring Resonator (SRR). Section 4 is dedicated to comparison of simulated and experimental results, with a specific focus on the radiation characteristics of the proposed design. Section 5 concludes with a discussion on manufacturing and testing, culminating in a comparison with existing designs cited in the bibliography.

## 2. DESIGN OF PROPOSED METAMATERIAL MULTI-BAND ANTENNA

The evolution of the proposed design and the corresponding $S$-parameter plots are illustrated in Figures 1 and 2, respectively. The antenna is fabricated on an FR4 substrate with a dielectric constant ($\varepsilon_r$) of 4.4 and a loss tangent ($\tan\delta$) of 0.02, and it has a thickness of 1.6 mm. The design evolution process of the proposed antenna is presented in tabular form in Table 1.

From Figure 2 and Table 1, it is noticed that the proposed design achieves resonance in a penta-band configuration, catering to the following wireless standards: 5G Sub-6 GHz NR Bands (5G FR1-n41: 2.496–2.690 GHz, n46: 5.15–5.925 GHz, n47: 5.855–5.925 GHz, n53: 2.483–2.495 GHz, n102: 5.925–6.425), WiMAX (3.65 GHz), WLAN (2.4/5.0/5.8), upper X band (7.67–12.28 GHz), and lower KU band (12.87–14.86 GHz), as illustrated in Figure 2. The operational band from 2.37 to 3.04 covers S band (2.4 GHz; WLAN: IEEE 802.11g) and 5G FR1 NR Band (n41) wireless communication applications. The second resonating band, spanning 3.58–4.12 GHz, is allocated to S band (3.65 GHz; WiMAX: IEEE 802.16e) wireless standards. The third resonating bands at 4.64–6.68 GHz are associated with C band (5.0/5.8 GHz; WLAN: IEEE 802.11a/j) wireless applications. The fourth

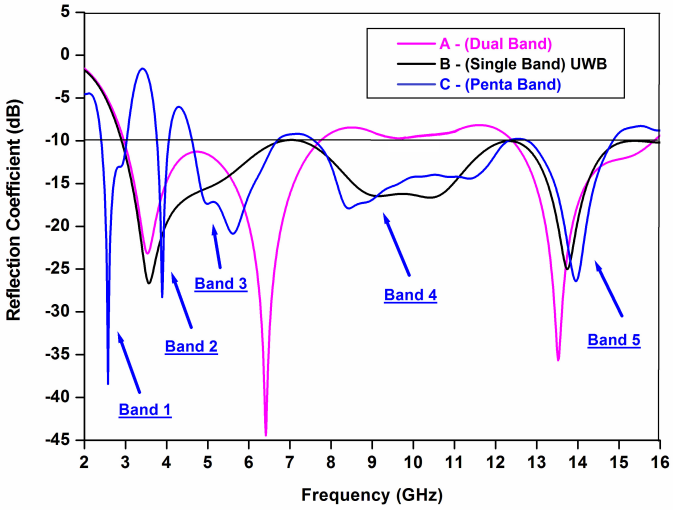


**FIGURE 2**. $S$ parameter $S_{11}$ (Sim) plots of design evolution steps.

**TABLE 1**. Design evolutionary stages of proposed structure.

| Design evolutionary stages | Patch and ground formation | Operating band (in GHz) | Covered Wireless Standards | Bandwidth (in %) | Peak Gain (in dBi) | Efficiency (in %) | Achieved wireless applications | Reasons |
|---|---|---|---|---|---|---|---|---|
| A | Patch: an octagonal shape Ground: Rectangular shape (DGS) | 2.96–7.72 | UWB band | 89.14 | 2.62 | 78.61 | No. of Applications — 2 Dual band (WLAN, WiMAX, interior Ku band) | An octagonal shape radiating patch and DGS ground part provide the wideband characteristics. |
| | | 12.43–15.86 | Lower Ku band | 24.25 | 3.11 | 82.57 | | |
| B | Patch: Slotted fractal based octagonal shape Ground: Rectangular slotted | 2.88–15.21 | UWB band, X-Band | 136.32 | 2.42 | 71.38 | No. of Applications — 1 Single band (Ultra wideband) | The current perturbation effect is produced because of the slotted patch area and ground. |
| C | Patch: Introducing the SRR cell with slotted radiating part Ground: Rectangular slotted | 2.37–3.04, | WLAN (2.4 GHz), 5G NR bands (n41: 2.496–2.690 GHz, n53: 2.483–2.495 GHz) | 24.77, | 2.36, | 63.56, | No. of Applications — 5 Penta band WLAN, WiMAX, X band, (5G Sub-6 GHz NR Bands (5G FR1) and Lower $K_U$ band | The Slotted fractal based patch is attached with SRR cell, which is responsible to create the current perturbations effect as well as negative permeability characteristics, to achieve the penta band resonating state regarding various wireless applications including 5G NR bands. |
| | | 3.58–4.12, | WiMAX (3.65 GHz) | 14.03, | 2.72, | 71.07, | | |
| | | 4.64–6.68, | WLAN (5.0 GHz), 5G NR bands (n46: 5.15–5.925 GHz) | 36.04, | 3.41, | 48.42, | | |
| | | | WLAN (5.8 GHz), 5G NR bands (n47: 5.855–5.925 GHz, n102: 5.925–6.425) | | 3.12, | 69.82, | | |
| | | 7.67–12.28, | X-band (8–12 GHz) | 46.21, | 3.18 | 72.87, | | |
| | | 12.87–14.86 | Lower Ku band (14.01 GHz) | 14.35 | 4.38 | 86.23 | | |

operating mode covers the entire X band for Satellite communication, radar, terrestrial broadband, and space communication applications. The fifth resonating band of the proposed antenna design, ranging from 12.87 to 14.86 GHz, is relevant to the Lower Ku band for molecular rational spectroscopy applications.

After design evolution of the proposed metamaterial penta band antenna design (Configuration — C) is illustrated in Figure 3, with all the optimized parameters listed in Table 2. The simulation process for the proposed design is carried out using CST Microwave Studio (CST MWS) software [35]. The fabricated prototype of the proposed antenna, including upper and lower sectional views, is depicted in Figure 4.

The experimental results are obtained using the measurement setup shown in Figure 5. The antenna structure exhibits penta-band resonating characteristics, as illustrated in Figure 6, with the corresponding bandwidth and $S$-parameter ($S_{11}$) values detailed in Table 3. Both the simulated and measured $S$-

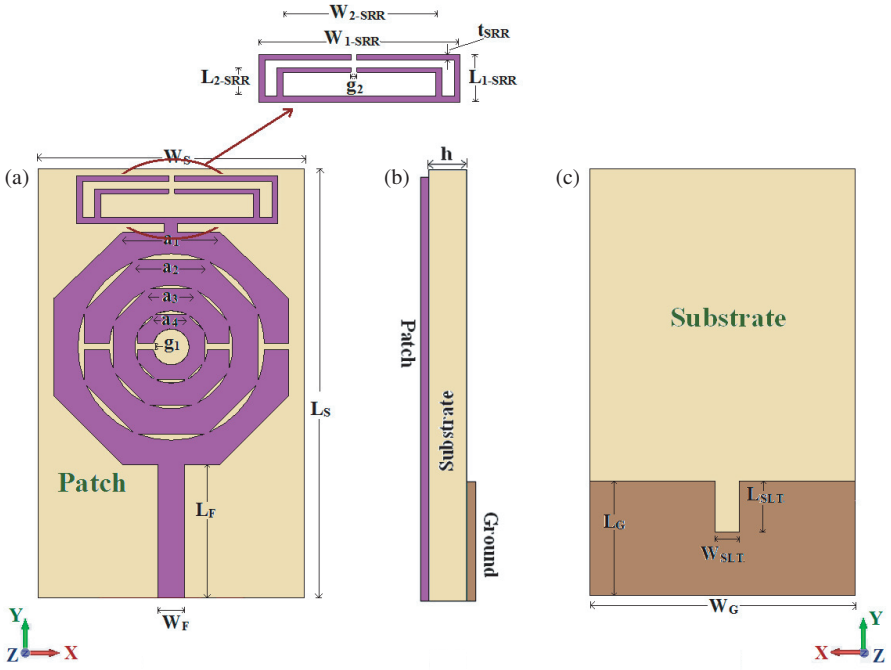


**FIGURE 3**. Configuration and prototype of the proposed structure.

**TABLE 2**. Optimized dimensions of the proposed design (in mm).

| $L_S$ | $W_S$ | h | $L_F$ | $W_F$ | $a_1$ | $a_2$ | $a_3$ | $a_4$ |
|---|---|---|---|---|---|---|---|---|
| 37 | 22 | 1.6 | 12 | 3.16 | 8 | 6 | 4 | 2.5 |
| $L_{1-SRR}$ | $W_{1-SRR}$ | $L_{2-SRR}$ | $W_{2-SRR}$ | $g_1$=$g_2$ | $W_G$ | $L_G$ | $L_{SLT}$ | $W_{SLT}$ |
| 4.5 | 17 | 3.5 | 13 | 0.5 | 22 | 10.5 | 5 | 3 |

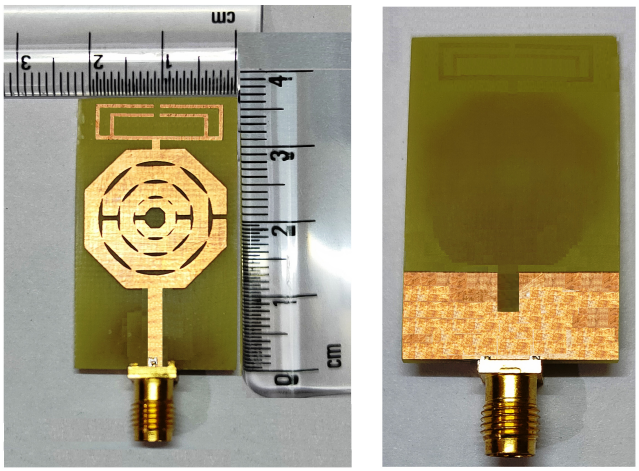

**FIGURE 4**. Proposed antenna fabricated prototype (upper and lower sectional view).

parameters ($S_{11}$) of the proposed structure are also presented in Figure 6. There are discrepancies between the simulated and measured $S_{11}$ results, likely caused by fabrication tolerances and cable losses. Yet, despite these imperfections, the overall agreement is undeniable, confirming the penta-band resonating mode. The impedance matching is optimized, but the lingering mismatch serves as a reminder that precision, even in its best form, is elusive.

### 2.1. Antenna Parametric Study

To confirm the desired working mechanism of proposed antenna with optimized dimensions, parametric observations are conducted with respect to the feed line ($L_F$ and $W_F$), ground ($L_G$ and $W_G$), SRR ($L_{1\text{-SRR}}$ and $W_{1\text{-SRR}}$), and hexagonal slotted patch dimensions (branch length ($a_1$) and gap ($g_1$)), and respective comparative reflection coefficient graphs are represented in Figures 7–10. The effect of feed line dimensions on the antenna reflection coefficient characteristics for different values of feed line length $L_F$ (9.0, 10.0, 11.0, 12.0, 13.0 mm) and width $W_F$ (2.5, 3, 3.16, 3.5, 4.0 mm) is depict in Figure 7. It is noticed that the improved impedance matching at the desired three resonating bands is achieved with the optimized value of feed line length $L_F = 12$ mm and $W_F = 3.16$ mm. With the increasing value of $L_F$, the fourth and fifth resonance bands represent the improved impedance matching characteristics at higher frequency range (7 to 14 GHz), and also, the first, second, and third resonance bands are inflated with reduced impedance matching at lower frequency range (2 to 6 GHz). The value of $W_F$ decreases, and impedance matching is enhanced at higher frequency range (8 to 16 GHz) for fourth and fifth resonance bands

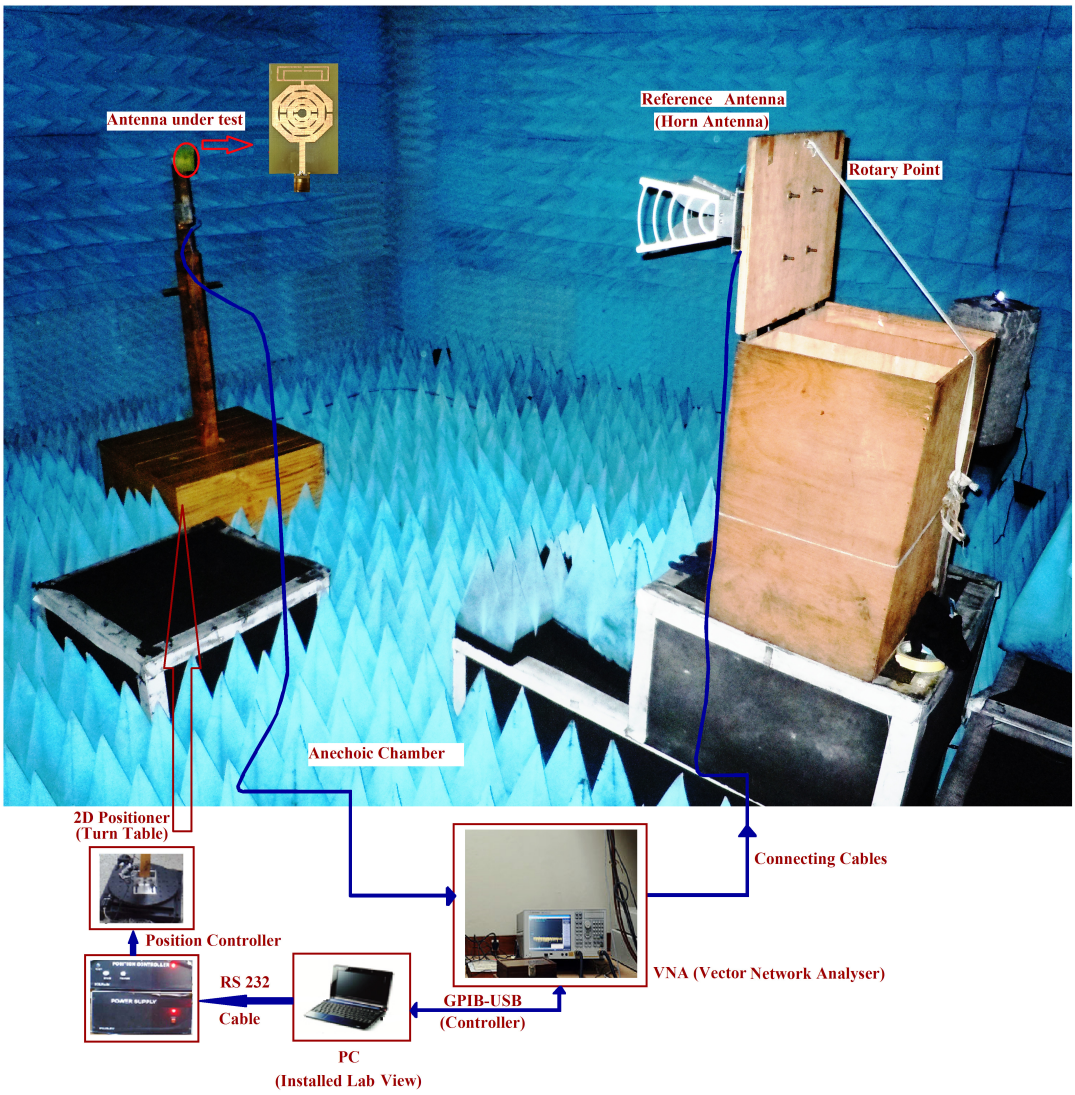


**FIGURE 5.** Antenna measurement setup.

**TABLE 3.** Comparison of the simulated and measured results of proposed penta-band antenna.

| Sr. No. | Operating Bands (in GHz) | | Bandwidth (in %) | | Wireless Standards | Wireless Applications |
|---|---|---|---|---|---|---|
| | Sim. | Exp. | Sim. | Exp. | | |
| 1 | 2.37–3.04 | 2.35–3.01 | 24.77% | 24.63% | (i) S band | WLAN (2.4 GHz; IEEE 802.11g) |
| | | | | | (ii) 5G NR bands | n41 (2.496–2.690 GHz), n53 (2.483–2.495 GHz) |
| 2 | 3.58–4.12 | 3.64–4.06 | 14.03% | 10.91% | (i) S band | WiMAX (3.65 GHz) |
| 3 | 4.64–6.68 | 4.65–6.52 | 36.04% | 33.48% | (i) C band | WLAN (5.0/5.8 GHz; IEEE 802.11 a/j) |
| | | | | | (ii) 5G NR bands | n46 (5.15–5.925 GHz), n47 (5.855–5.925 GHz), n102 (5.925–6.425 GHz) |
| 4 | 7.67–12.28 | 7.67–12.23 | 46.21% | 45.83% | (i) X-Band | Satellite communication, radar, terrestrial broadband, space communication |
| 5 | 12.87–14.86 | 13.01–14.88 | 14.35% | 13.41% | (i) Lower Ku band | Molecular rational spectroscopy |

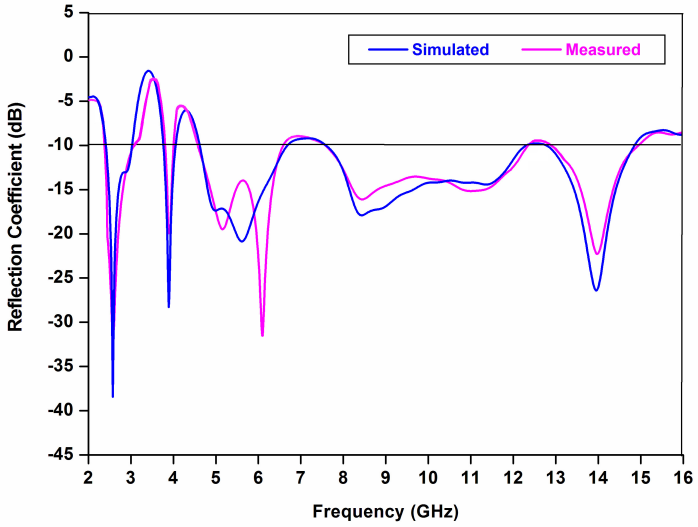


**FIGURE 6**. Comparison of simulated and experimental $S_{11}$ results of the proposed antenna.

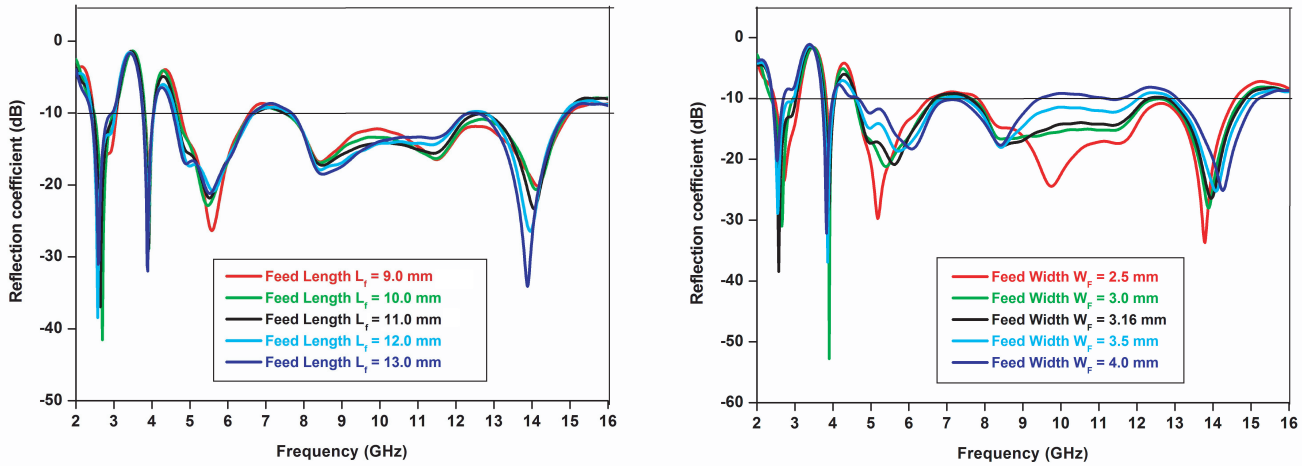


**FIGURE 7**. Comparative observation regarding feedline dimensions ($L_F$ and$W_F$).

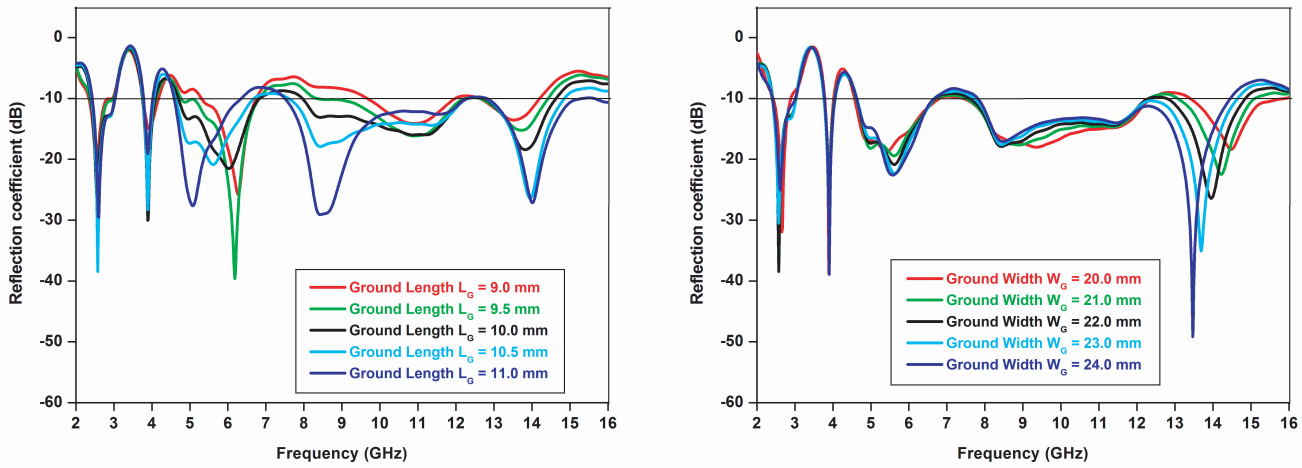


**FIGURE 8**. Comparative observation regarding ground dimensions ($L_G$ and $W_G$).

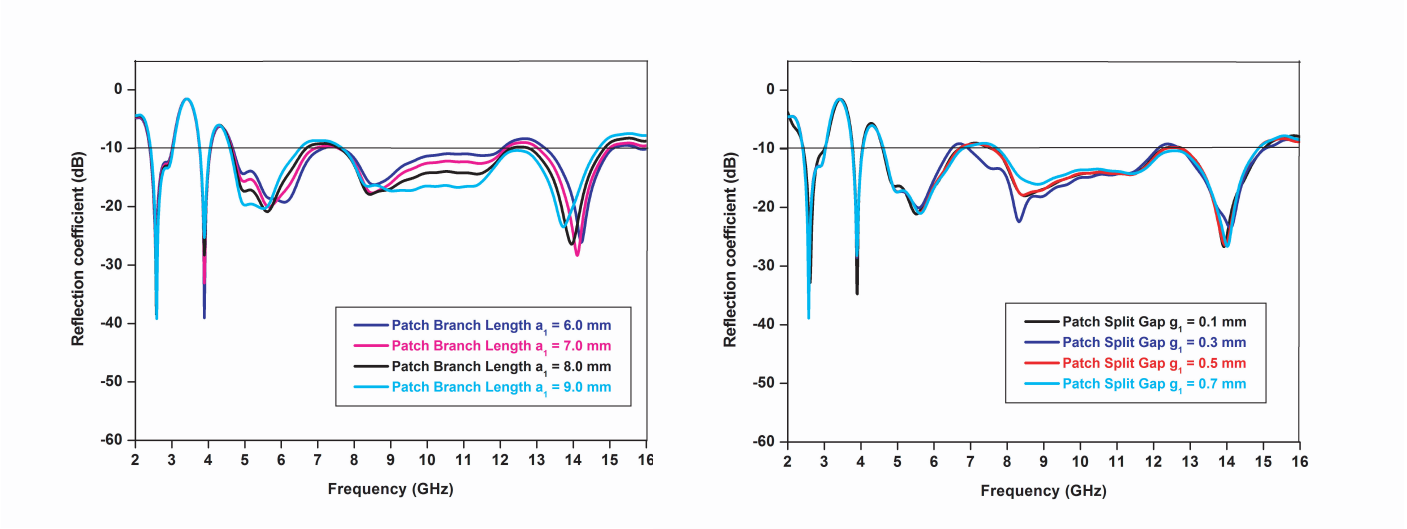


**FIGURE 9**. Comparative observation regarding patch dimensions (branch length $a_1$ and gap $g_1$).

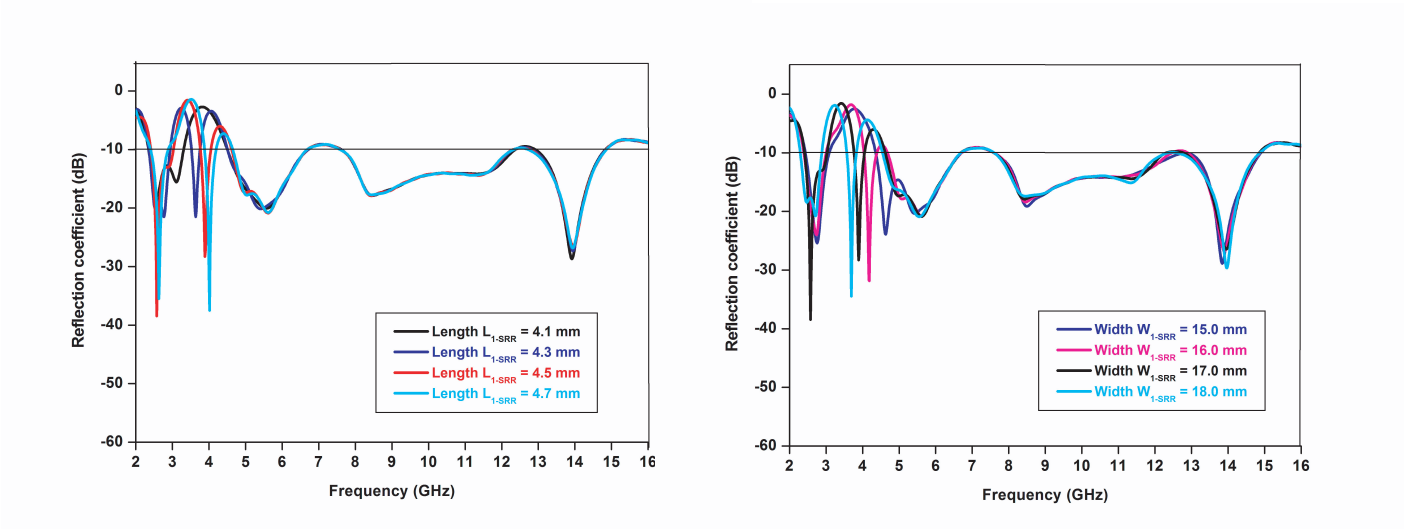


**FIGURE 10**. Comparative observation regarding SRR dimensions (length $L_{1\text{-SRR}}$ and width $W_{1\text{-SRR}}$).

as compared to the first, second, and third resonance bands. Preferred triple bands have been obtained at the optimized feed line dimensions ($L_F = 12$ mm and $W_F = 3.16$ mm).

Figure 8 illustrates the investigation of antenna performance based on variations in ground dimensions (length $L_G$: 9.0, 9.5, 10.0, 10.5, 11.0 mm; width $W_G$: 20.0, 21.0, 22.0, 23.0, 24.0 mm). It is observed that increasing the values of $L_G$ or $W_G$ improves the impedance matching for the fourth and fifth operating bands at higher frequencies. The proposed design achieves the desired penta-band characteristics with better impedance matching at the ground dimensions of $L_G = 10.5$ mm and $W_G = 22$ mm.

The parametric investigation also includes the observation of the antenna performance with respect to the patch dimensions (branch length $a_1$ and split gap $g_1$), as depicted in Figure 9. The parametric values of patch dimensions ($a_1$ and $g_1$) vary from 6.0 to 9.0 mm and 0.1 to 0.7 mm, respectively. The proposed structure resonates in tetra-band mode for split gap values of $g_1$ (0.1 and 0.3 mm) and branch length values of $a_1$ (6 and 9 mm). A penta-band mode with proper impedance matching is achieved with $g_1$ values of 0.5 and 0.7 mm and $a_1$ values of 7 and 8 mm. The branch length $a_1 = 8$ mm and split gap $g_1 = 0.5$ mm are chosen from the results, covering the desired penta operating band features with good impedance matching.

The effect of antenna performance (reflection coefficient) on the proposed SRR dimensions are shown in Figure 10. The variation of SRR length $L_{1\text{-SRR}} = 4.1$ to 4.7 mm and width $W_{1\text{-SRR}} = 15.0$ to 18.0 mm with a constant interval of 0.2 and 1.0 mm, respectively. It is seen that a small variation in $L_{1\text{-SRR}}$ and $W_{1\text{-SRR}}$ produces a observable shift in first, second, and third resonances, and better reflection coefficient behavior with good impedance matching is observed at $L_{1\text{-SRR}} = 4.5$ mm and $W_{1\text{-SRR}} = 17.0$.

## 2.2. Equivalent Circuit Formation

This section discusses the design of an equivalent model regarding proposed structure, integrating inductive ($L$), and capacitive ($C$) components as depicted in Figure 11. The expressions for $L$ and $C$ components are defined in Equations (1) and (2)

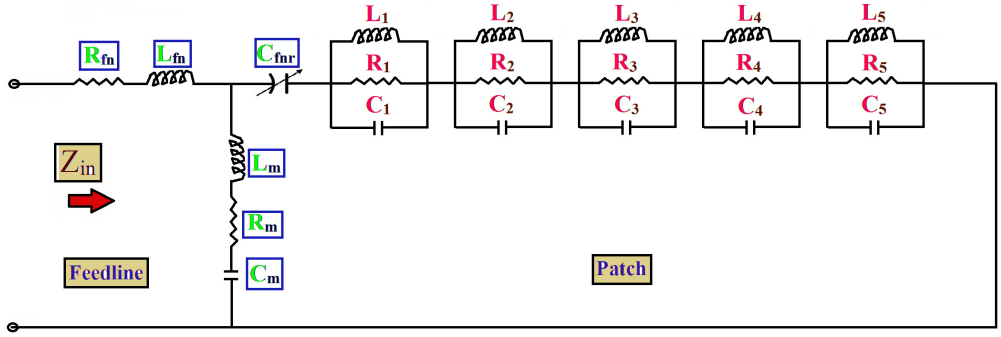


**FIGURE 11**. Equivalent circuit of proposed design.

below.

$$L = 0.0021 l_{the}\left[\ln\left\{(2l_{the})/(w_{the}+t_{hkk})\right\} + \frac{1}{2} + 0.2243\left\{(w_t he + t_{hkk})/(l_{the})\right\}\right] \quad (1)$$

$$C = (S_{Arpl}\varepsilon_o\varepsilon_r)/d_{spl} \quad (2)$$

where $l_{the}$ = length (cm), $w_{the}$ = width (cm), $t_{hkk}$ = thickness (mm), $S_{Arpl}$ = surface area of the plates, $d_{spl}$ = distance between the plates and $\varepsilon$ = permittivity of the medium.

The proposed antenna structure exhibits multiple excited modes to cover various wireless standards by applying a feed line across the octagonal-shaped miniaturized fractal radiating geometry. The central fractal radiating section generates the fundamental mode and higher odd modes with maximum values, as this section has a high impedance. Conversely, even modes (second and fourth order) are generated with minimal values in the central fractal radiating geometry and maximum values across the metamaterial cell (SRR). When feeding the proposed fractal radiating section, odd and even modes are excited by applying high and low impedance sources, respectively. These excited even and odd modes contribute to the antenna's effective multiband frequency response.

According to Characteristic Mode Theory (CMT), the surface current on the antenna conductor, $\mathbf{J_{CSUC}}$, can be expressed as a linear superposition of characteristic mode currents, $\mathbf{J_{CSUC}}$, as follows:

$$\mathbf{J_{CSUC}} = \sum_q [\alpha_{qaw}\mathbf{J_{CMUC}}] \quad (3)$$

where $\alpha_{qaw}$ is the MWC of the $q$th characteristic mode [40].

For an ideal conductor surface, the tangential component of the electric field, $\mathrm{P_{tangnt}}$ (J), generated by the induced currents, is equal in magnitude and opposite in direction to the incident electric field on the conductor surface, $(\mathbf{E_{in}})_{\mathrm{tangnt}}$, as expressed in the following equation:

$$\mathrm{P_{tangnt}}(\mathrm{J}) = (\mathbf{E_{in}})_{\mathrm{tangnt}}, \quad (4)$$

Equation (4) represents the formation between the source and field components. Putting the surface current value from Equation (3) into Equation (4) yields

$$\sum_q [\alpha_{qaw} P_{\mathrm{tangnt}}(\mathbf{J_{CMUC}})] = (E_{\mathrm{in}})_{\mathrm{tangnt}}$$
$$\sum_q [\alpha_{qaw} P_{\mathrm{tangnt}}(\mathbf{J_{CMUC}})] - (E_{\mathrm{in}})_{\mathrm{tangnt}}] = 0. \quad (5)$$

Equation (5) may be represented in another form by implementation of dot product and parameter $\mathbf{J}_{ki}$ ($k$ is any integer) as:

$$\sum_q \alpha_{qaw}\langle J_{ki} P_{\mathrm{tangnt}}\mathbf{J_{CMUC}}\rangle - \langle J_{ki}(E_{\mathrm{in}})_{\mathrm{tangnt}}\rangle = 0, \quad (6)$$

The characteristic impedance $Z = R + jX$ is defined with the combination of real and imaginary parts which are related to radiated and stored energy, respectively.

The characteristic modes exhibit the following orthogonality properties [40]:

$$\langle J^*_{ki} P_{\mathrm{tangnt}}\mathbf{J_{CMUC}}\rangle = (1+j\lambda_{qap})\delta_{tqaw} = P_{\mathrm{compx}}(J_{ki}, \mathbf{J_{CMUC}}), \quad (7)$$

where $\delta_{tqaw}$ = Kronecker Delta, $\lambda_{qap}$ = Eigen value corresponding to mode $q$, and $P_{\mathrm{compx}}$ ($\mathbf{J}_{ki}$, $\mathbf{J_{CMUC}}$) = Generated complex power.

On solving Equations (4) and (5), we can get

$$\alpha_{qaw} = \left[\langle \mathbf{J_{CMUC}}(E_{\mathrm{in}})_{\mathrm{tangnt}}\rangle/(1+j\lambda_{qap})\right] \quad (8)$$

From above Equation (8), it is observed that the modal weight coefficient $\alpha_{qa}$ is a complex number and may be expressed in matrix form as follows

$$\alpha_{qaw} = [V_{\mathrm{excitan}}]^T [I_{\mathrm{chcck}}]_n/(1+j\lambda_{qap}), \quad (9)$$

where $V_{\mathrm{excitan}}$ = Excitation source column matrix (obtain by the number of grids), and $I_{\mathrm{chcck}}$ = Characteristic current column matrix of mode $q$ (obtain by an eigenvalue equation).

The total current column matrix $I_{\mathrm{chcc}}$ of the conductor surface can be expressed as [40],

$$[I_{\mathrm{chcck}}] = \sum_q \left\{[V_{\mathrm{excitan}}]^T [I_{\mathrm{chckc}}]_q/(1+j\lambda_{qap})\right\}[I_{\mathrm{chcck}}]_q \quad (10)$$

The five excited modes, observed at resonant frequencies of 2.4, 3.65, 5.0, 5.8, 8.56, and 14.01 GHz, correspond to different

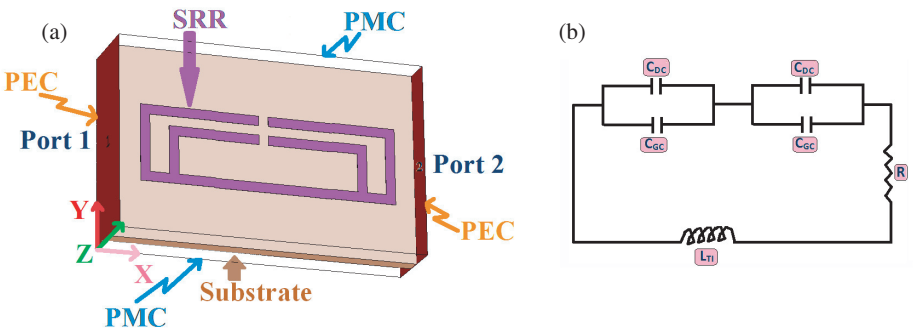


**FIGURE 12**. (a) Waveguide arrangement for proposed metamaterial SRR cell, (b) an equivalent model.

eigenvalues. While each mode is distinct, they are commonly associated with specific wireless standards. For these excited resonance modes, impedance matching is achieved through the octagonal fractal-shaped radiating element and the metamaterial cell (SRR) integrated into the proposed design. The input impedance of the structure is calculated by analyzing the electromagnetic fields between the radiating patch and ground plane. Each resonating mode can thus be represented by a general parallel resonant RLC circuit, with the equivalent input impedance expressed in Equation (11) [41]:

$$(Z_{\text{inputimp}})_{\text{equivlt}}(f) = j\omega_{\infty} + \sum_{i=1}^{N} [Rr, i/(1+j)Qu, i\{(f/f_{r-i})(f_{r-i}/f)\}] \quad (11)$$

where $(Z_{\text{inputimp}})_{\text{equivlt}}$ = Equivalent input impedance at feed point of the antenna, $L_{\infty}$ = Equivalent Inductance at higher frequency bands, $N$ = Number of radiating resonant modes, $f_{r,i}$ = Resonant frequency of the $i$th mode, $Q_{u,i}$ = $Q$-factor of $i$th resonant mode, $R_{r,i}$ = Radiation resistance of the $i$th mode, and $\omega = 2\pi$ (resonant frequency in radian/second).

## 3. PARAMETRIC EXTRACTION OF PROPOSED METAMATERIAL SRR

The proposed modified rectangular split ring resonator (RSSR) unit cell and its equivalent model are represented in Figure 12. The proposed cell is composed by two rectangular shape metallic rings with a split gap. The various parameters like effective material parameters (permeability $\mu_{\text{eff}}$/permittivity $\varepsilon_{\text{eff}}$), refractive index ($n$), and wave impedance ($z$) are derived by the implementation of the waveguide setup. In this setup, the proposed cell is placed between the input and output waveguide ports at the center position along the waveguide length. The waveguide ports are applied along the $x$-direction whereas the perfect electric conductor (PEC) and perfect magnetic conductor (PMC) boundary conditions are present along the $y$ and $z$-directions, respectively. To retrieve the simulated $S$ parameters ($S_{11}$ and $S_{12}$), the waveguide setup is established in simulation mode with the help of simulator CST Microwave Studio (MWS) [35], as depicted in Figure 12. The equivalent model of proposed SRR cell consists of an LC circuit. The inductive effect (inductance $L_{TI}$) and capacitive effect (capacitance $C_{GC}/C_{DC}$) of SRR are generated because of conducting ring and split gap/slots between the conducting rings respectively. To observe the experimental $S$ parameters ($S_{11}$ and $S_{12}$), the respective waveguide setup is designed in measurement mode with the help of adapters and VNA [37].

The electromagnetic wave is applied at port 1 and propagates through the rectangular metallic rings. Due to this, the conduction current is produced and flows through the outer ring to inner ring via gap. This gap and the metallic section are responsible for generating the inductive and capacitive effect (distributed capacitance) of SRR, respectively. The LC effect creates the resonant frequency as follows [38];

$$f_{\text{resonant-SRR}} = \frac{1}{2\pi\sqrt{L_{\text{total-equv}}C_{\text{total-equv}}}} \quad (12)$$

where

$$L_{\text{total-equv}} = 0.0002\left[\{2\left(L_{\text{Extrn-SRR}} + W_{\text{Exten-SRR}}\right) - g_1\}\left\{(\log_e 8)\frac{\left(L_{\text{Extrn-SRR}} + W_{\text{Exten-SRR}} - 0.5g_1\right)}{t_{\text{SRR}}}\right\} - Q\right] \quad (13)$$

$$C_{\text{total-equv}} = 0.5\left[\{\left(L_{\text{Extrn-SRR}} + W_{\text{Exten-SRR}}\right) - \pi\left(t_{\text{SRR}} + 0.5g'\right) - g_1\left(0.3 \times 10^{-8}\right)\left(\sqrt{\varepsilon}_e/Z_0\right)\} + \left\{\left(8.85 \times 10^{-12}\right)h' t_{\text{SRR}}/g_1\right\}\right] \quad (14)$$

where $L_{\text{Extrn-SRR}} \times W_{\text{Extrn-SRR}} \times h'$ = Volume of proposed SRR cell, $g_1$ = Split gap, $t_{\text{SRR}}$ = Thickness, $Q$ = Constant (2.4512), $g'$ = Rectangular SRR ring's gap, $\varepsilon_e$ = Effective permittivity of the medium, $Z_0$ = Characteristic impedance.

The effective dielectric parameter (permeability: $\mu_{\text{effect-med-par}}$) of the proposed SRR metamaterial structure is calculated with the help of the following equations [38, 39];

$$\mu_{\text{effect-med-par}} = n_{\text{ref-index}} \times z_{impd} \quad (15)$$

where

$$\textit{Refractive index}\ (n_{\text{ref-index}}) = (1/k_{wn}P_{\text{slab}})\cos^{-1}\left[(0.5/S_{21})\{((S_{21})^2 - (S_{11})^2 + 1\}\right] \quad (16)$$

$$\textit{Impedance}\ (z_{impd}) = \left[\{(1 + 2S_{11}) + (S_{11})^2 - (S_{21})^2\}\right.$$

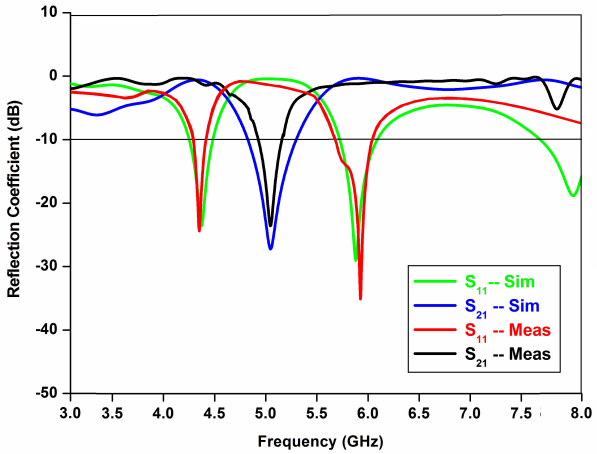


**FIGURE 13**. Comparison plots of Transmission ($S_{11}$) and Reflection ($S_{21}$) characteristics of the SRR cell.

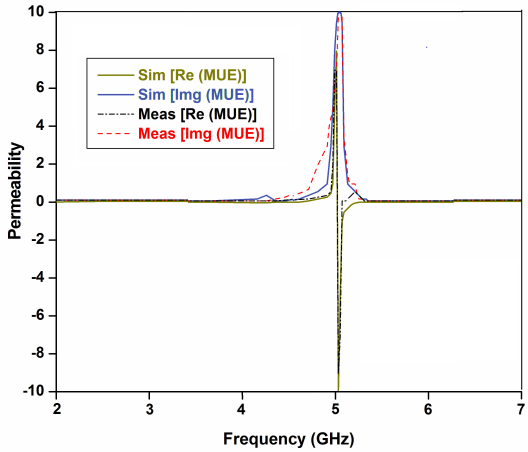


**FIGURE 14**. The negative permeability of the proposed SRR metamaterial cell.

$$/\{(1-2S_{11})+(S_{11})^2-(S_{21})^2\}^{1/2} \tag{17}$$

$$Wave\ number\ k_{\text{wnb}} = (\omega)/(3\times 10^8\ \text{m/s})$$

$$Slab\ (substrate\ material)\ thickness = P_{\text{slab-sb}}$$

The metamaterial characteristics of the proposed SRR structure are validated from its $S$ parameter plots (transmission: $S_{21}$ and reflection coefficients: $S_{11}$) in simulation as well as measurement mode (from waveguide setup). Figures 13 and 14 present the comparison of the transmission/reflection plots and the negative permeability characteristics plots of the SRR, respectively. It is noticed that the transmission peak (from Figure 13) and negative permeability characteristics (from Figure 14) of proposed metamaterial cell are identified at 5.01 GHz.

Parameters $S_{11}$ and $S_{21}$ have zero value (near $<\ -2$ dB level) and below $-10$ dB value (near $-28$ dB level), respectively, at the operating frequency 5.01 GHz, which indicates the stopband characteristics of proposed SRR at this desired frequency. The effective permeability curve represents the negative value at resonant frequency 5.01 GHz as shown in Figure 14.

In the design evolution of the proposed antenna, configuration C features a modified rectangular SRR structure placed in the radiating section and attached to a slotted fractal patch, enabling penta-band resonating characteristics (as shown in Figures 1 and 2). As discussed in Section 3 of the manuscript (Parametric Extraction of the Proposed Metamaterial SRR), the proposed metamaterial cell is responsible for generating an additional operating band at 5.01 GHz for WLAN (IEEE 802.11a) applications. The introduction of the metamaterial structure, which exhibits negative permeability characteristics (as shown in Figure 14), allows the antenna to achieve multiband functionality by loading the modified rectangle-shaped metamaterial cell. The design parameters of the proposed rectangular SRR geometry for the resonant frequency $f_1$ are determined by the following equation:

$$\begin{aligned}&\text{PERIM-SRR-Ext}\\ &= 2\left(L_{\text{1-SRR}}+W_{\text{1-SRR}}-g_2\right)\end{aligned}$$

$$= \frac{c}{2f1\sqrt{\varepsilon_{\text{effct}}}} = \frac{\lambda_{guwl}}{2} \tag{18}$$

$$\varepsilon_{\text{effct}} = (1/2)(\varepsilon r+1)+\frac{\left(\frac{1}{2}\right)(\varepsilon r-1)}{\sqrt{1+\frac{12h_{\text{substra}}}{W}}_{\text{feedwid}}} \tag{19}$$

Here, $P_{\text{ERIM-RSRR-Ext}}$ represents the perimeter of the external modified rectangular split rings, which is a function of length ($L_{\text{1-SRR}}$), width ($W_{\text{1-SRR}}$), and gap ($g_2$), as shown in Figure 3(a). For the proposed SRR to resonate at $f_1$, the external perimeter ($P_{\text{MRSRR-Ext}}$) should be approximately equal to half of the guided wavelength ($\lambda_{\text{guWl}}$) at the corresponding frequency. Additionally, the effective dielectric constant ($\varepsilon_{\text{effct}}$) is calculated using Equation (10), which depends on the substrate height ($h_{\text{substra}}$), feed line width ($W_{\text{feedwid}}$), and relative permittivity of the substrate ($\varepsilon_r$) [38].

## 4. PROPOSED ANTENNA MEASURED RESULTS AND DISCUSSIONS

The simulated surface current vector distributions on the conducting section of the proposed design at 2.42, 3.65, 5.01, 5.83, 8.45, and 14.01 GHz are plotted in Figure 15.

At the 2.42 GHz operating band, the current distribution is primarily concentrated across the feed line section, slotted radiation section, SRR cell, and the strip attached between the patch and SRR structure. As the frequency increases to 3.65 and 5.01 GHz, the radiation is primarily influenced by the modified rectangular SRR, with some current present around the outermost octagonal-shaped ring of the slotted patch, as shown in Figure 15. At higher frequencies, specifically 5.83, 8.45, and 14.01 GHz, most of the surface current is concentrated on the octagon-shaped patch (slotted rings) of the proposed antenna. This indicates that at higher frequencies, the proposed design achieves broadband performance with good impedance matching characteristics [40–45].

The comparative graphs of antenna peak gain and radiation efficiency (simulated and measured) are plotted in Figures 16

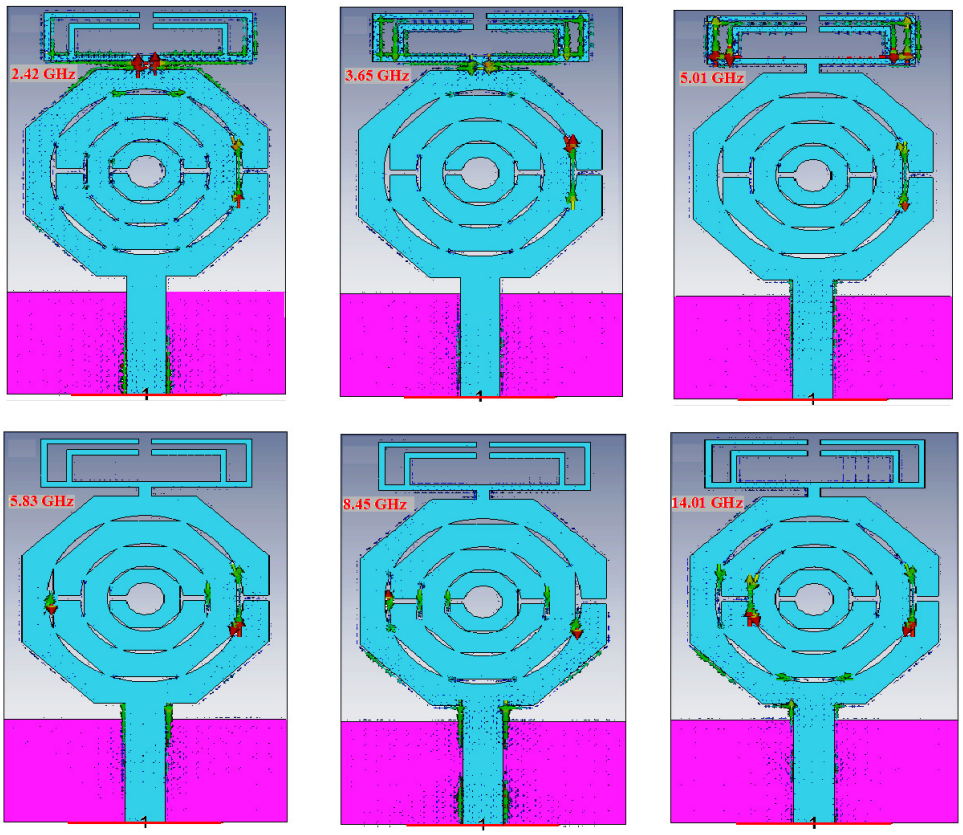


**FIGURE 15**. Surface Current distribution at 2.42, 3.65, 5.01, 5.83, 8.45, and 14.01 GHz during simulation mode.

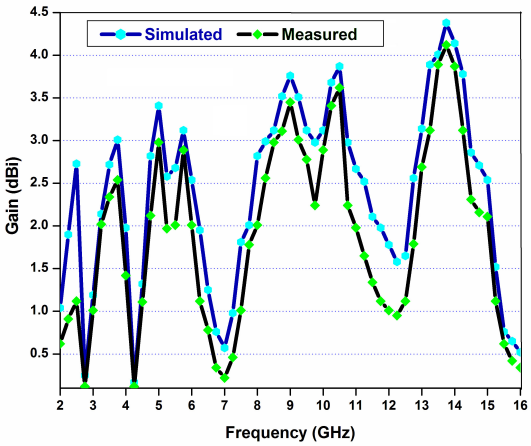


**FIGURE 16**. Comparative graphs of antenna peak gain (simulated and measured).

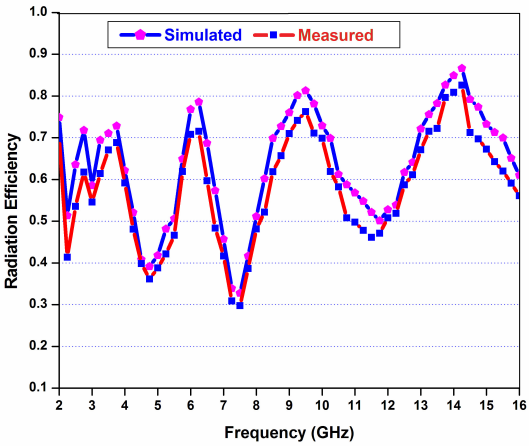


**FIGURE 17**. Comparative graphs of antenna radiation efficiency (simulated and measured).

and 17, respectively, and represented in tabular form in Table 4. The peak gain value and radiation efficiency of proposed design are 4.38 dBi and 86.23% respectively at Lower Ku band (14.01 GHz). It can be concluded from Figure 17 and Table 4 that the antenna achieves an average efficiency of over 70% across all resonant modes.

Figure 16 illustrates the peak gain plots of the proposed antenna design, both simulated and measured ones. The antenna achieves peak gain values, both simulated and measured ones, of 2.36, 2.72, 3.41, 3.12, 3.18, and 4.38 dBi for resonant modes of 2.4, 3.65, 5.0, 5.8, 8.56, and 14.01 GHz, respectively. Additionally, the measured gain values are 1.12, 2.34, 2.98, 2.89, 2.76, and 4.12 dBi for the corresponding resonant modes. Figure 17 presents the simulated and measured radiation efficiency plots. In the simulation, the proposed design demonstrates radiation efficiencies of 63.56%, 71.07%, 48.42%, 69.82%, 72.87%, and 86.23% at operating frequencies of 2.4, 3.65, 5.0, 5.8, 8.56, and 14.01 GHz, respectively.

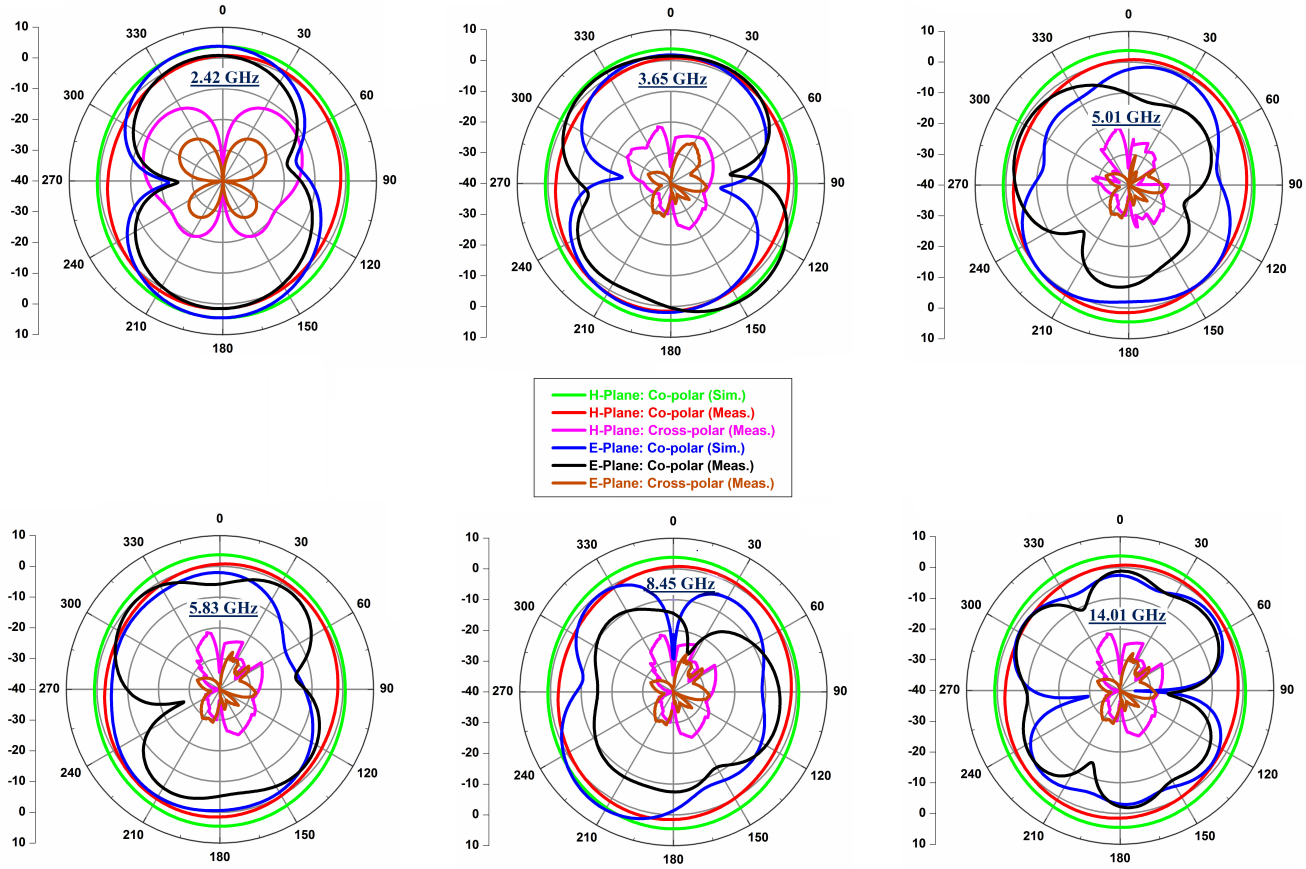


**FIGURE 18**. Patterns (Sim. & Meas.) at 2.42, 3.65, 5.01, 5.83, 8.45, and 14.01 GHz.

**TABLE 4**. Comparative analysis of antenna peak gain and radiation efficiency.

| Wireless standards | Antenna peak gain (in dBi) | | Radiation efficiency (in %) | |
|---|---|---|---|---|
| | Simulated | Experimental | Simulated | Experimental |
| WLAN (2.4 GHz) | 2.36 | 1.12 | 63.56 | 53.54 |
| WiMAX (3.65 GHz) | 2.72 | 2.34 | 71.07 | 67.32 |
| WLAN (5.0 GHz) | 3.41 | 2.98 | 48.42 | 41.69 |
| WLAN (5.8 GHz) | 3.12 | 2.89 | 69.82 | 62.12 |
| X-band (8.56 GHz) | 3.18 | 2.76 | 72.87 | 68.78 |
| Lower Ku band (14.01 GHz) | 4.38 | 4.12 | 86.23 | 82.28 |

Correspondingly, in measurements, the radiation efficiencies are observed to be 53.54%, 67.32%, 41.69%, 62.12%, 68.78%, and 82.28% for the respective operating frequencies.

Figure 18 displays the simulated and experimental far-field normalized $E$ & $H$ plane patterns (co-polarization and cross-polarization). It is apparent from the plot that the proposed antenna exhibits an omnidirectional and dipole like/bi-directional radiation pattern in the $H$-plane and $E$-plane (co-polarization mode), respectively. This comparison confirms the alignment between the simulated and experimental formations. To further analyze and study the radiation characteristics, the proposed design underwent testing in an anechoic chamber. The performance of the antenna is evaluated across wireless communication modes at frequencies of 2.4, 3.65, 5.0, 5.8, 8.56, and 14.01 GHz. At these frequencies, both the simulated and experimental results exhibit stability, resembling dipole-like characteristics in the $E$-plane, and omnidirectional behavior in the $H$-plane. Additionally, they demonstrate lower cross-polarization levels, typically below $-15$ dB [46–49]. The $E$ and $H$ plane patterns are analysed using an anechoic chamber. Inside the chamber, the far-field condition was considered, with the test antenna placed at a distance satisfying the Friis equation ($R \gg 2D^2/\lambda$) from the reference antenna. Measurements were conducted in step mode with 5° increments from 0° to 360°. This process was carried out for the $xy$ ($E$) and $yz$ ($H$) planes to obtain the $E$ and $H$ plane patterns, respectively, for

**TABLE 5**. A comparative analysis between existing antennas and the proposed antenna.

| Ref. | Year | Size ($mm^3$) | Fractional bandwidth (%) | Gain (dBi) | Efficiency (%) | Operating States | Applications Covered (GHz) |
|---|---|---|---|---|---|---|---|
| [11] | 2013 | $52.6 \times 30 \times 1$ | 47.27/38.88 | $-0.56/-0.62$ | 89.2/98.1 | 2 | GPS/WLAN (1.5/2.4) |
| [14] | 2018 | $32 \times 38 \times 1.6$ | 8/6/5/69.3 | 3.8 (Avg. Gain) | 89% (Avg. Rad. Eff.) | 4 | WLAN/WiMAX/ITU/X Band (2.4/3.35/5.8/7.5) |
| [22] | 2019 | $35 \times 34 \times 1.6$ | 11.81/4.27/4.29/6.62 /3.27/4.22/8.13 | 1.94/2.2/1.66/3.87 /3.65/4.06/4.14 | 41.5/48.6/58.1/60.1 /84.4/78.7/82.1 | 7 | WLAN/WiMAX/C/X /Ku Band (2.4/3/3.5/ 5/5.8/11.8/13.1) |
| [40] | 2020 | $30 \times 44 \times 1.6$ | 8.80/38.78 /15.54/35.45 | 2.63/2.58 /2.82/2.99 | 33.5/38.8 /84.4/72.8 | 4 | WLAN/WiMAX/WAVE/C /X Band (2.4/3.5/5.8/7.9) |
| [41] | 2020 | $9.5 \times 22 \times 1.6$ | 28.48/11.32/41.33/ 26.82/6.76/8.50/11.79 | 1.98/2.38/2.62/3.91 /2.24/3.28/4.11 | 51.25/54.28/59.69/67.82 /72.34/79.92/81.64 | 7 | WiMAX/Lower C band/ WLAN/Lower X band /Upper X band/Lower Ku band/Middle Ku band (3.5/4.41/5.8/8.26/ 10.48/13.35/14.42) |
| [50] | 2020 | $103.8 \times 68 \times 7$ | 58.39 | – | 41–69 | 1 | 5G Sub-6 GHz NR frequency Bands n77/n78/n79, LTE B46 |
| [51] | 2021 | $36 \times 32 \times 1.6$ | 84/85.32/35.45 /10.79/15.82 | – | – | 5 | LTE 2300/LTE 2500/Bluetooth /WLAN/WiMAX/ITU band (2.4/4.8/7.8/11.7/16.5) |
| [52] | 2021 | $50 \times 50 \times 0.8$ | 16.17/17.85/48.30 | 5.42/6.52/7.67 | – | 3 | Wi-Fi/WLAN/X-band (2.4/5.8/9.98) |
| [53] | 2022 | $150 \times 75 \times 0:8$ | 46.71 | 5.01 | 50–63 | 1 | 5G NR bands N77/N78/N79 (3.2–5.15 GHz) |
| [54] | 2022 | $150 \times 75 \times 7.8$ | 60.87 | – | 38–83 | 1 | 5G NR n77/n78/n79 and WLAN-5 GHz (3.2–6.0 GHz) |
| [55] | 2023 | $58.6 \times 58.6 \times 0.8$ | 14.08 | 4.8 | 76 | 1 | 5G NR n77 (3.3–3.8 GHz) |
| [56] | 2024 | $35 \times 30 \times 1.6$ | 40.8/22.3 | 3.87/3.93 | 80.12/82.34 | 2 | Wi-Fi, 5G NR communication, IoT Applications (3.5/5.3) |
| [57] | 2024 | $31.8 \times 27.6 \times 1.6$ | 43/25/15 | 1.5/4.1/6.5 | Less than 75 | 3 | 5G NR sub-band, X band, and Ku band (12–14 GHz) for upper resonance (3.5/8.5/13.7) |
| Proposed antenna | | $37 \times 22 \times 1.6$ | 24.77/14.03/36.04 /46.21/14.35 | 2.36/2.72/3.41 /3.18/4.38 | 63.56/71.07/48.42 /69.82/72.87/86.23 | 5 | S band WLAN (IEEE 802.11g)/ S band WiMAX (IEEE 802.16e)/ C band WLAN (IEEE 802.11a/j)/ X-Band (Satellite communication, radar, terrestrial broadband, space communication)/5G NR bands (n41: 2.496–2.690 GHz, n46: 5.15–5.925 GHz, n47: 5.855–5.925 GHz, n53: 2.483–2.495 GHz, n102: 5.925–6.425)/ Lower Ku band (Molecular rational spectroscopy) (2.4/3.65/5.0/5.8/8–12/) |

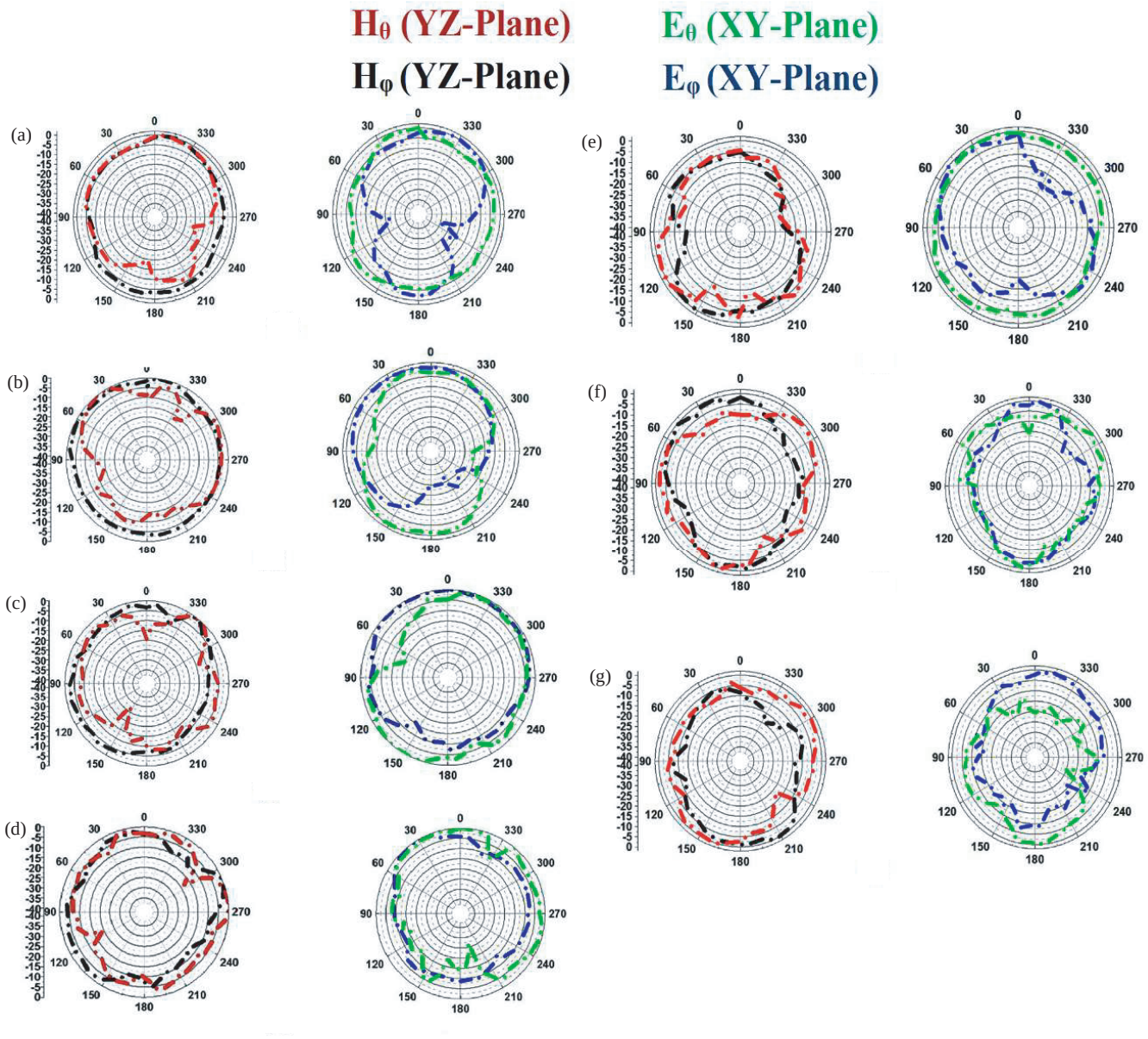


**FIGURE 19**. Measured $E$ and $H$-plane radiation patterns of the proposed design at (a) 2.42 GHz, (b) 3.65 GHz, (c) 5.01 GHz, (d) 5.83 GHz, (e) 8.45 GHz, (f) 13.35 GHz, and (g) 14.01 GHz.

both Co- and Cross-Polarization modes. The measured radiation characteristics of the antenna at the operating frequencies of 2.42, 3.65, 5.01, 5.83, 8.45, and 14.01 GHz for both the $xy$ ($E$) and $yz$ ($H$) planes are shown in Figure 18. It can be observed that the antenna exhibits an almost dipole-like pattern in the $xy$-plane and an omnidirectional pattern in the $yz$-plane. The glitches in the pattern at 5.01 GHz may be attributed to fabrication tolerances and cable losses, leading to some variations in the $E$-plane patterns between the simulated and experimental modes.

The radiation characteristics focus on examining the relative $E/H$ field strength of the antenna design. The patterns are identified for a single frequency, single polarization, and single plane cut. The $E$ and $H$ plane patterns are presented in either polar or rectilinear form with a dB strength scale. These patterns are measured in far-field mode inside an anechoic chamber using an a horn antenna (model No. LB-10180). The measured $E$ and $H$-plane radiation patterns of the proposed antenna design in the $x$-$y$ and $y$-$z$ planes, for both $\theta = 0°$ and $\varphi = 90°$, at the resonant frequencies 2.42, 3.65, 5.01, 5.83, 8.45, 13.35, and 14.01 GHz are shown in Figure 19. It is observed that the antenna exhibits stable radiation characteristics, with an omnidirectional pattern in the $yz$-plane ($H$) and a bi-directional radiation pattern in the $xy$-plane ($E$) at the respective resonant frequencies.

A comparative analysis of various characteristics of the proposed antenna is conducted in relation to previous literature, as illustrated in Table 5. It is evident from Table 5 that the proposed design offers enhanced antenna characteristics compared to those of existing antennas in the literature.

## 5. CONCLUSION

The proposed metamaterial inspired penta-band antenna for 5G Sub-6 GHz NR Bands and wireless applications WLAN/WiMAX/X-band/Lower Ku band is designed, fabricated, and tested. The antenna presents compactness in size with dimensions of $37 \times 22 \times 1.6\,\text{mm}^3$ and operates over penta-band mode at 2.37–3.04 GHz, 3.58–4.12 GHz, 4.64–6.68 GHz, 7.67–12.28 GHz, and 12.87–14.86 GHz to cover the wireless standards 5G New Radio (n41/n46/n47/n53/n102), WLAN (2.4 GHz), WiMAX (3.65 GHz), WLAN (5.0/5.8 GHz), and X-band (8–12 GHz). The structure exhibits a reasonable gain and more than 70% average radiation efficiency for all the resonance bands. The simulated results are on par with the measured ones.

## ACKNOWLEDGEMENT

The authors express gratitude to Prof. S. K. Koul of CARE, IIT Delhi, India, for generously providing measurement facilities.

## REFERENCES

[1] Elsheakh, D. M. N., H. Elsadek, E. A. F. Abdallah, M. F. Iskander, and H. El-Hennawy, "Reconfigurable single and multiband inset feed microstrip patch antenna for wireless communication devices," *Progress In Electromagnetics Research C*, Vol. 12, 191–201, 2010.

[2] Bakariya, P. S., S. Dwari, M. Sarkar, and M. K. Mandal, "Proximity-coupled microstrip antenna for bluetooth, WiMAX, and WLAN applications," *IEEE Antennas and Wireless Propagation Letters*, Vol. 14, 755–758, 2014.

[3] Wu, R.-Z., P. Wang, Q. Zheng, and R.-P. Li, "Compact CPW-fed triple-band antenna for diversity applications," *Electronics Letters*, Vol. 51, No. 10, 735–736, 2015.

[4] Mehdipour, A., A.-R. Sebak, C. W. Trueman, and T. A. Denidni, "Compact multiband planar antenna for 2.4/3.5/5.2/5.8-GHz wireless applications," *IEEE Antennas and Wireless Propagation Letters*, Vol. 11, 144–147, 2012.

[5] Cao, Y. F., S. W. Cheung, and T. I. Yuk, "A multiband slot antenna for GPS/WiMAX/WLAN systems," *IEEE Transactions on Antennas and Propagation*, Vol. 63, No. 3, 952–958, 2015.

[6] Saraswat, R. K. and M. Kumar, "A frequency band reconfigurable UWB antenna for high gain applications," *Progress In Electromagnetics Research B*, Vol. 64, 29–45, 2015.

[7] Samsuzzaman, M., T. Islam, N. H. A. Rahman, M. R. I. Faruque, and J. S. Mandeep, "Compact modified swastika shape patch antenna for WLAN/WiMAX applications," *International Journal of Antennas and Propagation*, Vol. 2014, No. 1, 825697, 2014.

[8] Ali, T., M. M. Khaleeq, S. Pathan, and R. C. Biradar, "A multiband antenna loaded with metamaterial and slots for GPS/WLAN/WiMAX applications," *Microwave and Optical Technology Letters*, Vol. 60, No. 1, 79–85, 2018.

[9] Chaurasia, P., B. K. Kanaujia, S. Dwari, and M. K. Khandelwal, "Design and analysis of seven-bands-slot-antenna with small frequency ratio for different wireless applications," *AEU — International Journal of Electronics and Communications*, Vol. 99, 100–109, 2019.

[10] Zhu, J. and G. V. Eleftheriades, "Dual-band metamaterial-inspired small monopole antenna for WiFi applications," *Electronics Letters*, Vol. 45, No. 22, 1104–1106, 2009.

[11] Xu, H.-X., G.-M. Wang, Y.-Y. Lv, M.-Q. Qi, X. Gao, and S. Ge, "Multifrequency monopole antennas by loading metamaterial transmission lines with dual-shunt branch circuit," *Progress In Electromagnetics Research*, Vol. 137, 703–725, 2013.

[12] Alam, T., M. Samsuzzaman, M. R. I. Faruque, and M. T. Islam, "A metamaterial unit cell inspired antenna for mobile wireless applications," *Microwave and Optical Technology Letters*, Vol. 58, No. 2, 263–267, 2016.

[13] Daniel, S., R. Pandeeswari, and S. Raghavan, "A compact metamaterial loaded monopole antenna with offset-fed microstrip line for wireless applications," *AEU — International Journal of Electronics and Communications*, Vol. 83, 88–94, 2018.

[14] Rao, M. V., B. T. P. Madhav, T. Anilkumar, and B. P. Nadh, "Metamaterial inspired quad band circularly polarized antenna for WLAN/ISM/Bluetooth/WiMAX and satellite communication applications," *AEU — International Journal of Electronics and Communications*, Vol. 97, 229–241, 2018.

[15] Anguera, J., C. Puente, C. Borja, and J. Soler, "Fractal shaped antennas: A review," *Encyclopedia of RF and Microwave Engineering*, 2005.

[16] Chen, H.-D., H.-W. Yang, and C.-Y.-D. Sim, "Single open-slot antenna for LTE/WWAN smartphone application," *IEEE Transactions on Antennas and Propagation*, Vol. 65, No. 8, 4278–4282, 2017.

[17] Lee, S. H., Y. Lim, Y. J. Yoon, C.-B. Hong, and H.-I. Kim, "Multiband folded slot antenna with reduced hand effect for handsets," *IEEE Antennas and Wireless Propagation Letters*, Vol. 9, 674–677, 2010.

[18] Yuan, B., Y. Cao, and G. Wang, "A miniaturized printed slot antenna for six-band operation of mobile handsets," *IEEE Antennas and Wireless Propagation Letters*, Vol. 10, 854–857, 2011.

[19] Sharma, S. K., J. D. Mulchandani, D. Gupta, and R. K. Chaudhary, "Triple-band metamaterial-inspired antenna using FDTD technique for WLAN/WiMAX applications," *International Journal of RF and Microwave Computer-Aided Engineering*, Vol. 25, No. 8, 688–695, 2015.

[20] Ali, T. and R. C. Biradar, "A compact multiband antenna using λ/4 rectangular stub loaded with metamaterial for IEEE 802.11N and IEEE 802.16E," *Microwave and Optical Technology Letters*, Vol. 59, No. 5, 1000–1006, 2017.

[21] Kukreja, J., D. K. Choudhary, and R. K. Chaudhary, "CPW fed miniaturized dual-band short-ended metamaterial antenna using modified split-ring resonator for wireless application," *International Journal of RF and Microwave Computer-Aided Engineering*, Vol. 27, No. 8, e21123, 2017.

[22] Saraswat, R. K. and M. Kumar, "A metamaterial hepta-band antenna for wireless applications with specific absorption rate reduction," *International Journal of RF and Microwave Computer-Aided Engineering*, Vol. 29, No. 10, e21824, 2019.

[23] Ali, T., M. S. Aw, and R. C. Biradar, "A fractal quad-band antenna loaded with L-shaped slot and metamaterial for wireless applications," *International Journal of Microwave and Wireless Technologies*, Vol. 10, No. 7, 826–834, 2018.

[24] Pandeeswari, R. and S. Raghavan, "Broadband monopole antenna with split ring resonator loaded substrate for good impedance matching," *Microwave and Optical Technology Letters*, Vol. 56, No. 10, 2388–2392, 2014.

[25] Arora, C., S. S. Pattnaik, and R. N. Baral, "Srr inspired microstrip patch antenna array," *Progress In Electromagnetics Research C*, Vol. 58, 89–96, 2015.

[26] Rajeshkumar, V. and S. Raghavan, "SRR-based polygon ring penta-band fractal antenna for GSM/WLAN/WiMAX/ITU band applications," *Microwave and Optical Technology Letters*,

Vol. 57, No. 6, 1301–1305, 2015.
[27] Elavarasi, C. and T. Shanmuganantham, "Multiband SRR loaded Koch star fractal antenna," *Alexandria Engineering Journal*, Vol. 57, No. 3, 1549–1555, 2018.
[28] Ahmad, B. H. and H. Nornikman, "Fractal microstrip antenna with Minkowski island split ring resonator for broadband application," in *2013 IEEE International RF and Microwave Conference (RFM)*, 214–218, Penang, Malaysia, Dec. 2013.
[29] Hu, J.-R. and J.-S. Li, "Compact microstrip antennas using CSRR structure ground plane," *Microwave and Optical Technology Letters*, Vol. 56, No. 1, 117–120, 2014.
[30] Rajkumar, R. and K. U. Kiran, "A metamaterial inspired compact open split ring resonator antenna for multiband operation," *Wireless Personal Communications*, Vol. 97, 951–965, 2017.
[31] Saraswat, R. K. and M. Kumar, "Miniaturized slotted ground UWB antenna loaded with metamaterial for WLAN and WiMAX applications," *Progress In Electromagnetics Research B*, Vol. 65, 65–80, 2016.
[32] Saraswat, R. K. and M. Kumar, "A vertex-fed hexa-band frequency reconfigurable antenna for wireless applications," *International Journal of RF and Microwave Computer-Aided Engineering*, Vol. 29, No. 10, e21893, 2019.
[33] Liu, W.-C., C.-M. Wu, and Y. Dai, "Design of triple-frequency microstrip-fed monopole antenna using defected ground structure," *IEEE Transactions on Antennas and Propagation*, Vol. 59, No. 7, 2457–2463, 2011.
[34] Singh, S., A. Varshney, V. Sharma, I. T. Elfergani, C. Zebiri, and J. Rodriguez, "A compact off-set edge fed odd-symmetric hybrid fractal slotted antenna for UWB and space applications," *Progress In Electromagnetics Research B*, Vol. 102, 37–60, 2023.
[35] "Computer simulation technology microwave studio (CST MWS)," Retrieved from http://www.cst.co.
[36] Sivia, J. S., A. P. S. Pharwaha, and T. S. Kamal, "Analysis and design of circular fractal antenna using artificial neural networks," *Progress In Electromagnetics Research B*, Vol. 56, 251–267, 2013.
[37] Chen, H., J. Zhang, Y. Bai, Y. Luo, L. Ran, Q. Jiang, and J. A. Kong, "Experimental retrieval of the effective parameters of metamaterials based on a waveguide method," *Optics Express*, Vol. 14, No. 26, 12 944–12 949, 2006.
[38] Saha, C. and J. Y. Siddiqui, "Versatile CAD formulation for estimation of the resonant frequency and magnetic polarizability of circular split ring resonators," *International Journal of RF and Microwave Computer-Aided Engineering*, Vol. 21, No. 4, 432–438, 2011.
[39] Smith, D. R., S. Schultz, P. Markoš, and C. M. Soukoulis, "Determination of effective permittivity and permeability of metamaterials from reflection and transmission coefficients," *Physical Review B*, Vol. 65, 195 104–195 109, 2002.
[40] Saraswat, R. K. and M. Kumar, "A quad band metamaterial miniaturized antenna for wireless applications with gain enhancement," *Wireless Personal Communications*, Vol. 114, No. 4, 3595–3612, 2020.
[41] Saraswat, R. K. and M. Kumar, "Implementation of hybrid fractal metamaterial inspired frequency band reconfigurable multiband antenna for wireless applications," *International Journal of RF and Microwave Computer-Aided Engineering*, Vol. 30, No. 9, e22315, 2020.
[42] Agrawal, A., P. K. Singhal, and A. Jain, "Design and optimization of a microstrip patch antenna for increased bandwidth," *International Journal of Microwave and Wireless Technologies*, Vol. 5, No. 4, 529–535, 2013.
[43] Puri, I. and A. Agrawal, "Bandwidth and gain increment of microstrip patch antenna with shifted elliptical slot," *International Journal of Engineering Science and Technology*, Vol. 3, No. 7, 5539–5545, 2011.
[44] Maheshwari, S., P. Jain, and A. Agarwal, "CPW-fed wideband antenna with U-shaped ground plane," *International Journal of Wireless and Microwave Technologies*, Vol. 5, 25–31, 2014.
[45] Jain, A. and A. Agrawal, "Design and optimization of a microstrip patch antenna for increased bandwidth," *International Journal of Electronics and Communication Engineering*, Vol. 7, No. 2, 191–195, 2014.
[46] Vaswani, J. and A. Agarwal, "A four port, dual band antenna for fifth generation mobile communication and WLAN services," *Acta Technica Corviniensis — Bulletin of Engineering*, Vol. 13, No. 4, 73–76, 2020.
[47] Agarwal, A., M. Kumar, P. Jain, and S. Maheshwari, "Tapered circular microstrip antenna with modified ground plane for UWB communications," *International Journal of Electronics and Communication Engineering & Technology (IJECET)*, Vol. 4, No. 3, 43–47, 2013.
[48] Vaswani, J., "Dual-band, dual-polarized two element slot antenna for fifth generation mobile devices," *Turkish Journal of Computer and Mathematics Education (TURCOMAT)*, Vol. 12, No. 3, 4822–4830, 2021.
[49] Vaswani, J. and A. Agarwal, "Twelve-port dual-polarized dual-band mimo antenna for fifth-generation mobile devices," *ICTACT Journal on Communication Technology*, Vol. 12, No. 3, 2490–2497, 2021.
[50] Sim, C.-Y.-D., H.-Y. Liu, and C.-J. Huang, "Wideband MIMO antenna array design for future mobile devices operating in the 5G NR frequency bands n77/n78/n79 and LTE band 46," *IEEE Antennas and Wireless Propagation Letters*, Vol. 19, No. 1, 74–78, 2020.
[51] Bharti, G. and J. S. Sivia, "A design of multiband nested square shaped ring fractal antenna with circular ring elements for wireless applications," *Progress In Electromagnetics Research C*, Vol. 108, 115–125, 2021.
[52] Kaur, A. and P. K. Malik, "Multiband elliptical patch fractal and defected ground structures microstrip patch antenna for wireless applications," *Progress In Electromagnetics Research B*, Vol. 91, 157–173, 2021.
[53] Mu, W., Z. Wang, M. Yang, W. Nie, and P. Wang, "A six-port slot antenna system with wideband and high-isolation for 5G NR bands," *Progress In Electromagnetics Research M*, Vol. 107, 105–118, 2022.
[54] Jiang, J.-Y. and H.-L. Su, "A wideband eight-element mimo antenna array in 5G NR n77/78/79 and WLAN-5 GHz bands for 5G smartphone applications," *International Journal of Antennas and Propagation*, Vol. 2022, No. 1, 8456936, 2022.
[55] Murugan, C. and T. Kavitha, "A compact four-element modified annular ring antenna for 5G applications," *Progress In Electromagnetics Research C*, Vol. 137, 169–183, 2023.
[56] Xue, J., G. Wang, S. Li, Z. Wang, and Q. Liang, "A metamaterial based dual-band UWB antenna design for 5G applications," *Progress In Electromagnetics Research M*, Vol. 127, 85–92, 2024.
[57] Neeshu, K. and A. K. Tiwary, "A compact, high gain ring metamaterial unit cell loaded triple band antenna for 5G application," *Progress In Electromagnetics Research M*, Vol. 124, 99–106, 2024.
[58] Garg, S., P. Jain, S. Garg, B. Sharma, G. Das, N. Sardana, S. Kumar, and A. K. Singh, "Compact polarization-insensitive microwave metamaterial absorber with hepta-band characteristics,"

*Physica Scripta*, Vol. 99, No. 7, 075541, 2024.

[59] Samanta, S., G. P. Singh, P. Jain, A. K. Singh, and N. Sardana, "Arm angle dependence of X-shaped metamaterial resonator in the X-band regime," in *International Conference on Fundamental and Industrial Research on Materials*, 183–190, 2024.

[60] Jain, P., P. K. Sahoo, A. D. Khaleel, and A. J. A. Al-Gburi, "Enhanced prediction of metamaterial antenna parameters using advanced machine learning regression models," *Progress In Electromagnetics Research C*, Vol. 146, 1–12, 2024.

[61] Wang, L., L. Han, W. Guo, L. Zhang, C. Yao, Z. Chen, Y. Chen, C. Guo, K. Zhang, C.-N. Kuo, *et al.*, "Hybrid Dirac semimetal-based photodetector with efficient low-energy photon harvesting," *Light: Science & Applications*, Vol. 11, No. 1, 53, 2022.

[62] Viti, L., A. Politano, K. Zhang, and M. S. Vitiello, "Thermoelectric terahertz photodetectors based on selenium-doped black phosphorus flakes," *Nanoscale*, Vol. 11, No. 4, 1995–2002, 2019.

[63] Viti, L., J. Hu, D. Coquillat, W. Knap, A. Tredicucci, A. Politano, and M. S. Vitiello, "Black-phosphorus terahertz photodetectors," *Adv. Mater.*, Vol. 27, 5567–5572, 2015.

[64] Zhang, K., L. Han, Z. Hu, K. Xiao, M. Jiang, A. Yu, X. Pan, D. Wang, L. Zhang, X. Lv, and e. al., "Plasmonic architectures boosting performance in terahertz photodetectors," *Laser & Photonics Reviews*, Vol. 18, No. 6, 2301243, 2024.

[65] Xu, W., T. K. Lee, B.-S. Moon, H. Song, X. Chen, B. Chun, Y.-J. Kim, S. K. Kwak, P. Chen, and D.-H. Kim, "Broadband plasmonic antenna enhanced upconversion and its application in flexible fingerprint identification," *Advanced Optical Materials*, Vol. 6, No. 6, 1701119, 2018.

[66] Park, K.-D. and M. B. Raschke, "Polarization control with plasmonic antenna tips: A universal approach to optical nanocrystallography and vector-field imaging," *Nano Letters*, Vol. 18, No. 5, 2912–2917, 2018.

[67] Zak, A., M. A. Andersson, M. Bauer, J. Matukas, A. Lisauskas, H. G. Roskos, and J. Stake, "Antenna-integrated 0.6 THz FET direct detectors based on CVD graphene," *Nano Letters*, Vol. 14, No. 10, 5834–5838, 2014.

[68] Zhang, K., Z. Hu, L. Zhang, Y. Chen, D. Wang, M. Jiang, G. D'Olimpio, L. Han, C. Yao, Z. Chen, *et al.*, "Ultrasensitive self-driven terahertz photodetectors based on low-energy type-ii dirac fermions and related van der waals heterojunctions," *Small*, Vol. 19, No. 1, 2205329, 2023.

[69] Xu, H., C. Guo, J. Zhang, W. Guo, C.-N. Kuo, C. S. Lue, W. Hu, L. Wang, G. Chen, A. Politano, X. Chen, and W. Lu, "PtTe2-based type-II dirac semimetal and its van der waals heterostructure for sensitive room temperature terahertz photodetection," *Small*, Vol. 15, No. 52, 1903362, 2019.

[70] Tang, W., A. Politano, C. Guo, W. Guo, C. Liu, L. Wang, X. Chen, and W. Lu, "Ultrasensitive room-temperature terahertz direct detection based on a bismuth selenide topological insulator," *Advanced Functional Materials*, Vol. 28, No. 31, 1801786, 2018.